

Surface deployment of DAS systems: Coupling strategies and comparisons to geophone data

Nicholas Harmon¹  | Catherine A. Rychert¹  | John Davis¹ |
Gilberto Brambilla²  | William Buffet¹ | Ben Chichester¹ | Yuhang Dai¹  |
Petros Bogiatzis¹  | James Snook²  | Lieke van Putten² | Ali Masoudi² 

¹Ocean and Earth Science, University of Southampton, Southampton, UK

²Optoelectronics Research Centre, University of Southampton, Southampton, UK

Correspondence

Nicholas Harmon, Ocean and Earth Science, University of Southampton, Southampton, UK.
Email: n.harmon@soton.ac.uk

Funding information

Natural Environment Research Council, Grant/Award Numbers: NE/T005890/1, NE/S012877/1

Abstract

Distributed acoustic sensing (DAS) systems are a recent technological development for seismic observations over a broad range of frequencies with a wide variety of applications. Typically, fibre-optic cables are buried underground or cemented into well casings where the cables are well-coupled to the ground. Quick and temporary surface deployment of cables has great potential utility in areas where rapid surveying and minimal disturbance of the subsurface are desired. However, proper mechanical coupling between the fibre and the ground is still a challenge for temporary surface deployments. Here we test four different coupling strategies for a DAS system deployed in a grassy field, including uncoupled, pinned under tension to the ground, weighted down by carpeting, and weighted down by a sandbag. We compare the DAS data to vertical component geophone data and estimated horizontal geophone data to assess the fidelity of DAS ground motion recordings. We find a completely uncoupled fibre is capable of recording seismic energy up to ~10 m away from the source, while the pinned and weighted fibre record signals over several tens of metres. The DAS recordings compare favourably with the estimated horizontal displacement records from the multi-channel seismic system. There is a good agreement between the phase of the signals acquired by the DAS system with that of the geophones, but there is a mismatch of up to a factor of two in the absolute amplitude at some frequencies. We perform several standard analysis techniques, including refraction and multi-channel analysis of surface waves, on the coupled DAS data. Finally, the instrument response of the coupled DAS data to ground motions is determined using the estimated horizontal component from the multi-channel seismic system. Surface deployments of DAS systems provide a complementary set of observations to standard vertical geophone deployments, for instance, if multi-component geophones are not available. Also, there are some advantages in speed and ease of deployment of DAS in comparison to geophones depending on the coupling strategy used.

KEYWORDS

DAS, geophone, MASW, surface waves, velocity

This is an open access article under the terms of the [Creative Commons Attribution License](https://creativecommons.org/licenses/by/4.0/), which permits use, distribution and reproduction in any medium, provided the original work is properly cited.

© 2022 The Authors. *Near Surface Geophysics* published by John Wiley & Sons Ltd on behalf of European Association of Geoscientists and Engineers.

INTRODUCTION

Distributed acoustic sensing (DAS) is a recently developed method used to measure seismic wavefields with high spatial and temporal sampling using fibre-optic cables (Lindsey & Martin, 2021). DAS uses the phase of the Rayleigh backscattered light within the fibre-optic cable to estimate the optical fibre elongation with nano-strain precision along discrete sections of the fibre. If the fibre is embedded or coupled to a structure or the ground, this technique permits the measurement of motions and deformations of the medium that affects the fibre (Masoudi et al., 2013).

DAS systems can be deployed in a variety of settings and for various seismic and environmental applications. For example, vertical seismic profiling using a permanently deployed fibre behind the borehole casing has been used extensively for body wave measurements (Daley et al., 2016). In addition, submarine cables have been used to record earthquakes and detect tides (Lindsey et al., 2019; Marra et al., 2018; Masoudi et al., 2019; Zumberge et al., 1988). Unused telecommunication fibre, or dark fibre, has been used to examine near-surface seismic structure using surface waves in ambient noise as well as earthquakes and manmade sources (Ajo-Franklin et al., 2019; Dou et al., 2017; Milne et al., 2020; Zhu et al., 2021). Telecommunication fibre also has many useful applications for geotechnical engineering in urban environments (Ajo-Franklin et al., 2019; Dou et al., 2017; Martin et al., 2017; Zhu et al., 2021). Surface deployment of DAS systems has received less attention.

Surface deployment of DAS systems has many potential advantages, including, for instance, imaging of the subsurface beneath construction or archaeological sites. In certain settings, including archaeological sites or nature reserves, disturbing or damaging the ground is forbidden for preservation purposes. Laying fibre-optic cable along the ground at such sites may permit seismic surveys with minimal disturbance. Potentially rapid deployment and recovery of fibre over hundreds of metres has economic advantages for field crews. In addition, the sensitivity of DAS systems to 1-D elongation of the sensing fibre has the potential to provide complementary information to standard vertical component multi-channel seismic systems when three component sensors are not available, giving information about horizontal ground motions (Daley et al., 2016; Lindsey et al., 2020; Wang et al., 2018).

The coupling of the fibre to the ground is an important issue for surface deployments of DAS systems. Telecommunication optical fibres are designed to have minimal coupling with acoustic waves in the surrounding environment, and there are special cables (Freeland et al., 2017) to increase the optical fibre sensitivity to external vibrations. Vertical fibres are often encased in cement in oil and gas wells to enhance mechanical coupling

(Mestayer et al., 2011). In other cases, fibres are buried in horizontal trenches or pipes for protection (Jousset et al., 2018). Buried fibres in pipes have weaker mechanical coupling to the ground.

In surface deployments, the coupling between the fibre and ground may degrade due to vegetation or rough topography. Therefore, surface deployments may not experience the uniform elongation that a buried fibre might sense. DAS coupling can be increased, for instance, by using sandbags. DAS strain recordings of seismic signals from an experiment with sandbags placed every 9 m over the length of a 142.5 m fibre, with a gauge length of 10 m compare favourably with multi-channel geophone data (Spikes et al., 2019). Another study coupled the fibre to the ground by freezing the fibre in a trench and found improvements in signal recovery, but also found some complications in the signals (Yang et al., 2021). Overall, the success of these experiments suggests that further investigation into the viability of rapid and temporary surface deployments of optical fibre and optimal deployment strategies is warranted. Ideally, with good coupling, both accurate amplitude and phase information of the seismic wavefield can be recovered from surface DAS deployments. The phase information allows for many traditional techniques to be applied to estimate the seismic velocity. Accurate amplitude information is required for measurements of the seismic quality factor (Q-factor) of the near surface. Q-factor is useful for earthquake hazard assessment and various geotechnical engineering purposes (Cornell, 1968).

In this study, we examine four different surface coupling strategies for DAS systems and compare the results from the DAS system recordings to recordings from a 24-multi-channel vertical geophone seismic system. We then perform refraction and multi-channel analysis of surface waves (MASW) of the DAS and geophone waveforms to determine the subsurface properties. Comparison of the two verifies the applicability of using the DAS system for shallow geophysical applications. We also present an empirical transfer function for the DAS strain recordings to observed ground motions, which encapsulates the response of the fibre and its effective coupling to the ground.

METHODS

The location of the experiment was a grassy field with a densely packed fine-grained soil adjacent to the Highfield campus of the University of Southampton (Figure 1a). The fibre-optic cable was deployed along an inverted “L” shaped line, 30 m in the N-S direction and 12 m extending eastwards from the northernmost point of the main line (Figure 1b). This geometry allowed for the recording of two orthogonal horizontal components of the wavefield on the DAS system. The vertical geophones of the multi-channel array were deployed parallel

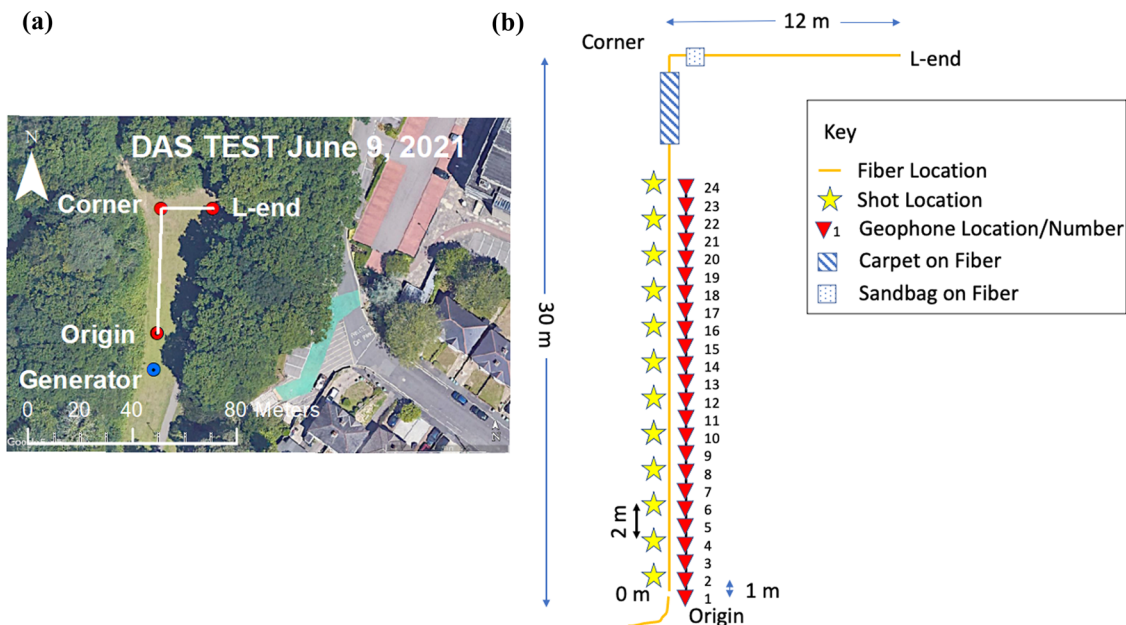


FIGURE 1 Map of the experiment region (a) and details of the geometry of the experimental set-up (b). Note the different coupling devices used for the fibre and their location in (b). Stars show shot locations, inverted red triangles show geophone locations, and sandbag and carpet locations are indicated by hatched rectangles. Fibre is indicated in yellow.

to the N-S-oriented leg and within 5 cm of the fibre. For the seismic source, we struck a 6.4 kg hammer onto a plastic block every 2 m located from 1 m to 23 m along the main line. We used 2 or 5 shots at each location, depending on the experiment.

For the DAS recording, we used the University of Southampton proprietary designed differential phase interrogator, capable of fully quantifying the changes in the fibre strain in real time (Chen et al., 2019). The phase analysis mechanism of the system was based on an imbalanced Mach-Zehnder interferometer (IMZI) with 8 m path imbalance, which corresponds to a 4-m gauge length (Masoudi & Newson, 2016). The role of the IMZI is to mix the backscattered signal from spatially separated points on the fibre. The phase of the mixed signal can then be used to measure the changes in the strain level at each point along the sensing fibre. The fibre used was a standard SMF-28 tight-buffer optical fibre with a 2-mm jacket. We used a 1550-nm seed laser, spatial sampling of 0.30 m, and a temporal sampling interval of 0.50 ms for the DAS system. Data were recorded for the duration of repeated shots at each location, which typically took about two minutes. The relatively low sampling rate was chosen to make handling of the continuously recorded DAS data more manageable. The DAS system acquisition parameters are summarized in Table 1.

For the geophone measurements, we used the Geometrics Geode multi-channel seismic system, with 24 vertical component geophones. The first geophone was located at the origin, and the rest were spaced every 1 m going northwards (Figure 1b). We recorded the shots

TABLE 1 Optical specification

Parameter name	Parameter value
MZI path imbalance	8 m
Spatial resolution (gauge length)	4 m
Channel spacing	30 cm
Pulse repetition period	500 μ s (\equiv 2 kHz)
Probe pulse duration	20 ns
Probe pulse wavelength	1550 nm
Pulse repetition period (sampling interval)	0.50 ms
Record length	Continuous, 30–120 s, cut to 0.256 s

TABLE 2 Multi-channel seismic specification

Parameter name	Parameter value
Geophone spacing	1 m
Sampling interval	0.125 ms
Recording length	0.256 s
Filtering	None
Gain	24 dB

at a 0.125 ms sampling interval, for a total of 0.256 s, with a gain of 24 dB. No filters or automatic gain control were applied at acquisition. The multi-channel acquisition parameters are summarized in Table 2.

We tested four different approaches of coupling the fibre to the ground during two shot series experiments. The first experiment was performed with the fibre

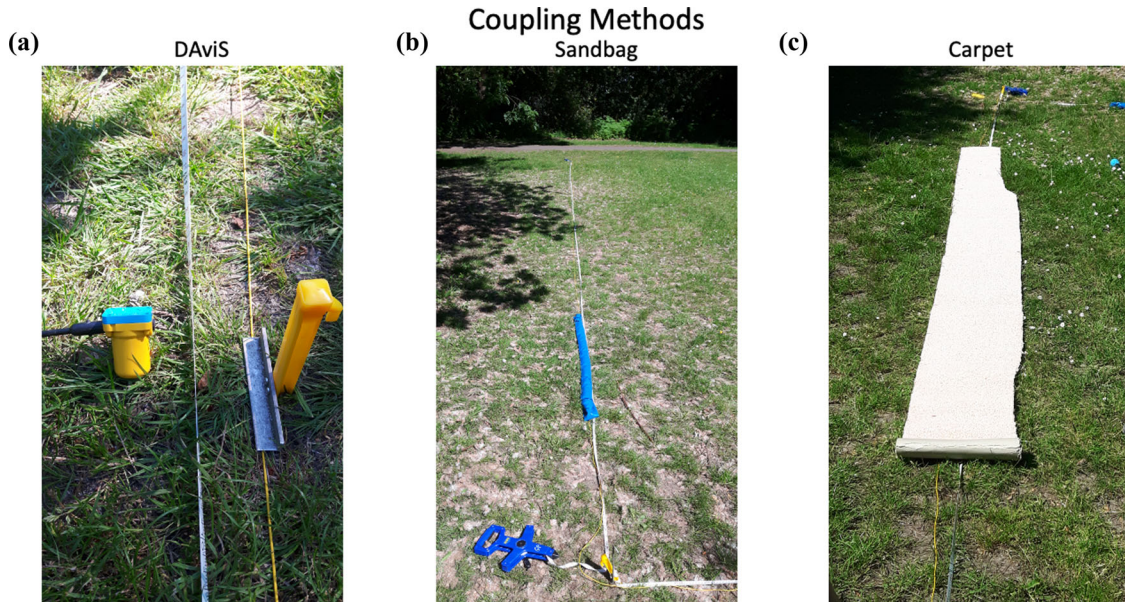


FIGURE 2 Pictures of coupling methods used on the fibre. (a) DAViS couplers used to pin the fibre to the ground under tension. (b) Sandbag deployed on fibre. (c) Carpet deployed on fibre

stretched out straight on the ground, but otherwise totally uncoupled. Two shots were performed at each location. In the second experiment, we coupled the fibre to the ground using three different methods: (1) pinning the pre-strained fibre to the ground under tension using a custom-made coupler (referred here after as DAViS coupler); (2) weighting the fibre down using 4 m of carpeting; and (3) weighting the fibre down using a 1-m-long sandbag (Figure 2). Five shots were performed at each location for this series. To ensure consistency between shots, we used the same operator for all shots. During the experiments, foot traffic on a nearby path varied with time, which may have affected the background noise slightly.

In the first experiment with an uncoupled fibre, we deployed the geophones vertically. In the second experiment, with coupled fibre, we started with the geophones deployed vertically. The experiment was then repeated with the geophones deployed at a $\sim 30^\circ$ angle from the vertical axis and parallel with the survey line. The multi-channel data using the two different geophone orientations were used to estimate the horizontal ground motion using the relationship:

$$H(t) = \frac{R(t) - V(t) \cos \theta}{\sin \theta}, \quad (1)$$

where $H(t)$ is the estimated horizontal time series as a function of time, t , $R(t)$ is the tilted component geophone deployed at an angle of θ to the vertical, and $V(t)$ is the vertical component geophone data in the same location. This was necessary as we did not have horizontal geophones available. However, it has been demonstrated that geophones deployed at an angle record mixed vertical and horizontal components of ground motion

despite some degradation due to harmonic distortion (Claassen et al., 2015). Tilted geophones have some loss of dynamic range (8%–50% at 40°) (Claassen et al., 2015). However, the geophones yield valid results as long as the tilt angles are less than the critical threshold where the solenoid coil and the mass are no longer inertial (Claassen et al., 2015). We estimate the critical angle to be 80° for the 14 Hz geophones used here (Claassen et al., 2015). We estimate the error in the $\sim 30^\circ$ deployment angle at $\pm 15^\circ$ and use this error range to quantify the error in the waveforms.

The DAS data were post processed. The phase information from the DAS data was processed and extracted in real time through arctan analysis (Masoudi & Newson, 2017). In this analysis, the variation in the intensity of three detectors at the output of the IMZI was used to measure the phase variation at 0.30 m intervals along the sensing fibre (Masoudi & Newson, 2017). The phase variation was then converted to strain using the following equation (Chen et al., 2019):

$$\Delta\varphi = 0.78 \varepsilon \ell \beta, \quad (2)$$

where ℓ is the gauge length, β is the propagation constant of light, and ε represents the strain exerted on the sensing fibre. Cycle skipping was visible in the raw strain data and corrected by removing the median using a moving window of 100 samples. This also removed the lowest frequency components of the data. The strain data were integrated spatially over one gauge length centred on the measurement point, to obtain displacement at each sensing channel. Shot time windows were manually picked, and shots from the same location were stacked after time alignment via cross-correlation.

Geophone data were pre-processed. We linearly stacked the vertical and the 30° geophone data for all the shots. The instrument response was then removed from the data in the spectral domain based on the manufacturer's specifications without calibration of the instruments. Specifically, the zeros and poles of the instrument response in counts/m/s were determined from the physical parameters of the system, e.g., mass, natural frequency, damping, coil resistance, etc. (Templeton, 2013). After response correction, the data were in units of ground velocity, so we integrated the data in time to determine the ground displacement. The source used had a dominant frequency higher than 14 Hz within the range where the geophone amplitude response was nominally flat, and the phase response was linear.

We performed refraction and MASW to estimate the velocity structure beneath our study area and to ascertain if the results from the DAS would be similar to the geophone data. We used refraction analysis of two flat layers to determine the P-wave velocity structure of the upper ~6 m using first arrivals picked from the shots at either end of the geophone array (Telford et al., 1990). We calculated frequency–phase velocity (f – v) diagrams using only the phase information of the DAS and geophone array to estimate Rayleigh wave phase velocities for fundamental and higher modes using a beamforming method (Harmon et al., 2008). We then forward modelled the fundamental and first three higher modes using the Computer Programs in Seismology package (Herrmann, 2013) to determine the S-wave velocity structure with a simple four-layered model, holding the P-wave structure fixed to the velocities determined by refraction in the upper two layers.

We also estimated an instrument response function for the fibre strain recorded by the DAS system. The goal was to directly convert DAS outputs to ground displacements by the simple linear filter given by the response function and to ascertain the frequency range over which the assumption of a linear relationship might hold. If the response has been determined, then the filter can be applied to the DAS data without the need to collect geophone data. We used spectral division of the DAS output and the nearest estimated horizontal ground motion from the geophone data for one stacked shot section with the shot location at 23 m.

The empirical response, $R(f)$, as a function of frequency (f) is given by:

$$R(f) = \frac{C_{DH}(f)}{C_{DD}(f)} \quad (3)$$

where C_{DH} is the cross spectra of the DAS and the estimated horizontal motion from the geophones, and C_{DD} is the auto spectra of the DAS. Thus, a spectral multiplication of the fibre strain data gives the equivalent inline (in the fibre longitudinal direction) horizontal displacement.

We resample the DAS data to the same sampling rate as the geophone data. We estimate the cross and auto spectra using the Hanning method, with 1024 samples and a 25% overlap in the windows (Oppenheim & Schaffer, 1975). Spectral coherence between the DAS and estimated horizontal components is also calculated using the Hanning method with the same parameters. Coherence is used to determine the frequency range over which the empirical response function is reliable (Bendat & Piersol, 2000). Coherence $\gamma(f)$, is given by the following expression:

$$\gamma(f) = \frac{|C_{DH}(f)|^2}{|C_{HH}(f)| |C_{DD}(f)|}, \quad (4)$$

where C_{HH} is the auto spectra of the horizontal component.

RESULTS

The comparison between the coupled fibre and uncoupled fibre is shown in Figure 3 with no normalization. A comparison with each trace normalized to a maximum of 1, for two different shot locations is shown in Figure 4. The normalization effectively enhances low amplitude phases and increases our ability to detect moveout on signals at larger distances. For these comparisons, we stack two shots per profile. On the uncoupled fibre, for the shot at 1 m from the origin (Figure 3a), moveout is visible along the fibre from 0–16 m of the 'L'. The amplitude drops off rapidly between 10 m and 16 m. In the normalized plot of the uncoupled fibre with the shot at 1 m (Figure 4a), some phases are visible out to 30 m distance and after the corner of the 'L', which have arrival times greater than 0.15 s. However, there is a lot of speckle with amplitudes near one, preceding the coherent signals at distances greater than 15 m, indicating a low signal-to-noise ratio (SNR). It is hard to determine if the phases visible at >16 m are coherent with the phases visible at <15 m distance since the energy is patchy. For the uncoupled fibre with the shot location at 21 m (Figures 3c and 4c), coherent phases are visible 10–15 m from the shot point in the unnormalized plots. In the normalized plots, phases are visible to 20 m away and past the corner of the 'L'. Again, a similar level of speckle is seen in the normalized plots, indicating a low SNR. The stacked shots at 1 m (Figure 3b) of the coupled fibre show a stronger signal visible at distances of 0–25 m, a region coupled with the DAVIS couplers. Beneath the carpet, the coupling appears to degrade, and no signal is visible. Yet, the signal is visible beneath the sandbag extending for ~4 m in total on either side of the sandbag deployment, visible between 0.15 s and 0.23 s. The signal may or may not be the coherent lower frequency Rayleigh waves visible on the

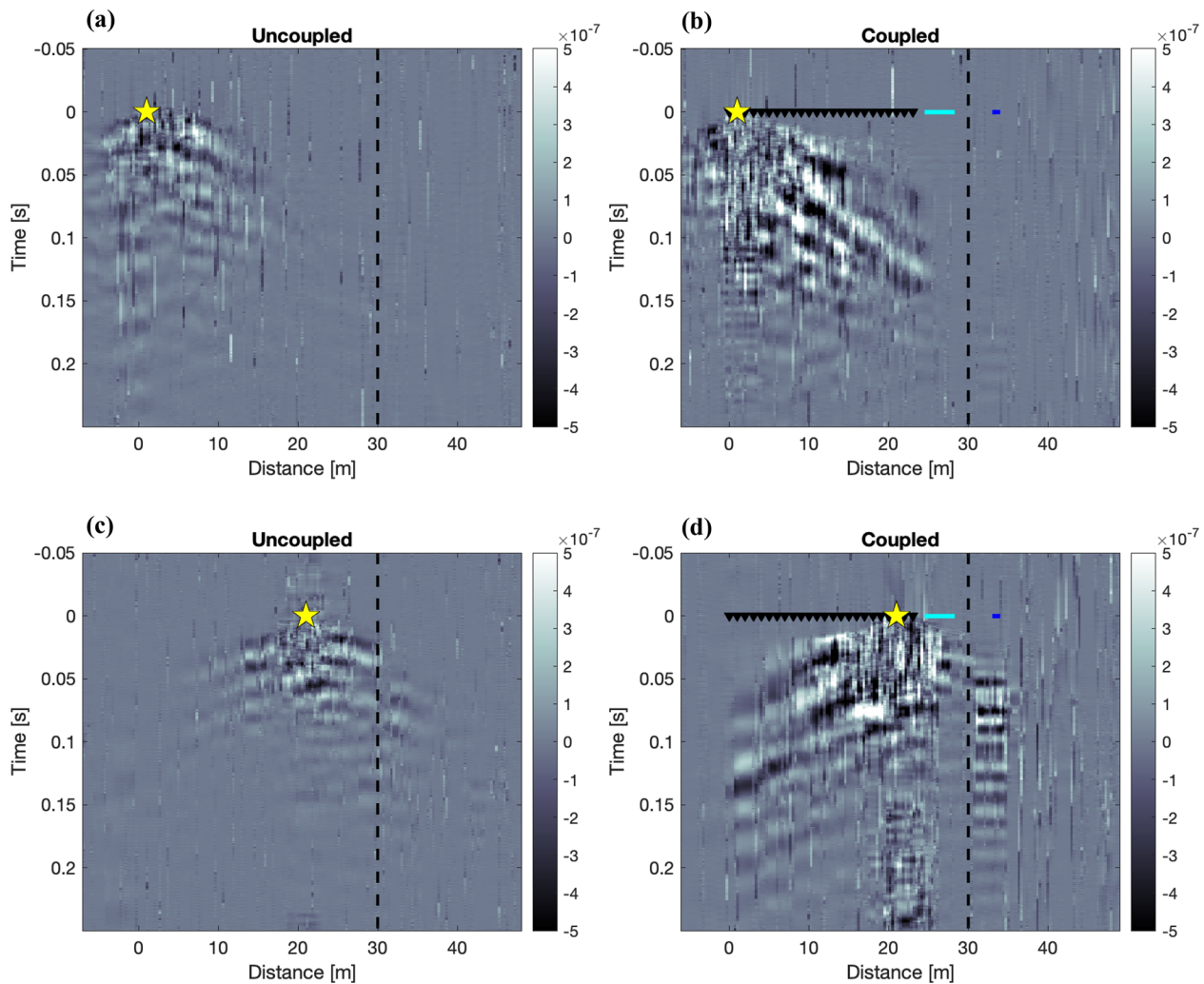


FIGURE 3 Uncoupled fibre (a, c) profiles and coupled fibre (b, d) profiles for two example shot locations: 1 m (a, b), 21 m (c, d). Stars indicate the source locations. Black triangles show locations of DAvis couplers, cyan line indicates the location of the carpet, and blue line indicates the location of the sandbag. Black dashed line shows the location of the corner of the ‘L’ geometry shown in Figure 1.

N-S section. The different (W-E) orientation of the line and resulting directivity of the sensitivity of the fibre may mean that it is sensing another part of the wavefield. The normalized plots of this shot (Figure 4b) show a very similar image to the unnormalized plots. There is little coherent energy beneath the carpet, although the signals beneath the sandbag are more visible. For the coupled fibre with a shot at 21 m, there is a strong signal recorded by the DAS, from 0–30 m of the ‘L’ and beneath the sandbag in both the unnormalized and normalized records (Figures 3d and 4d). The energy beneath the carpet coupling decreases in amplitude at 0.10 s for this shot.

Beneath the sandbag in both shots, the phases do not have the same arrival times as the phases visible on the N-S line at the same geometric distance. There is no moveout visible in the phases, and they appear rather flat with increasing distance along the line. In addition, the signal appears to have a higher

dominant frequency. This is partly due to the change in the geometry and possibly because the fibre may sense a different horizontal component of the wavefield. Specifically, for the shots shown, the difference in geometric distance from the shot is < 1 m for 30–35 m along the line. The fibre orientation beneath the sandbag is also nearly orthogonal to the shot, so the fibre is likely recording strains associated with any horizontally polarized shear waves generated by the shot. In addition, the 1 m sandbag may cause more uniform strain along its length, which makes the phase arrival appear to have less moveout.

Overall, the P-wave phase is more visible in the coupled examples than the uncoupled examples (Figures 3 and 4). The P-wave is the first arriving coherent energy in these figures. Rayleigh waves are also more visible in the coupled examples (Figures 3 and 4). They can be identified as phases with different moveout visible for different frequencies. Some of the energy visible within

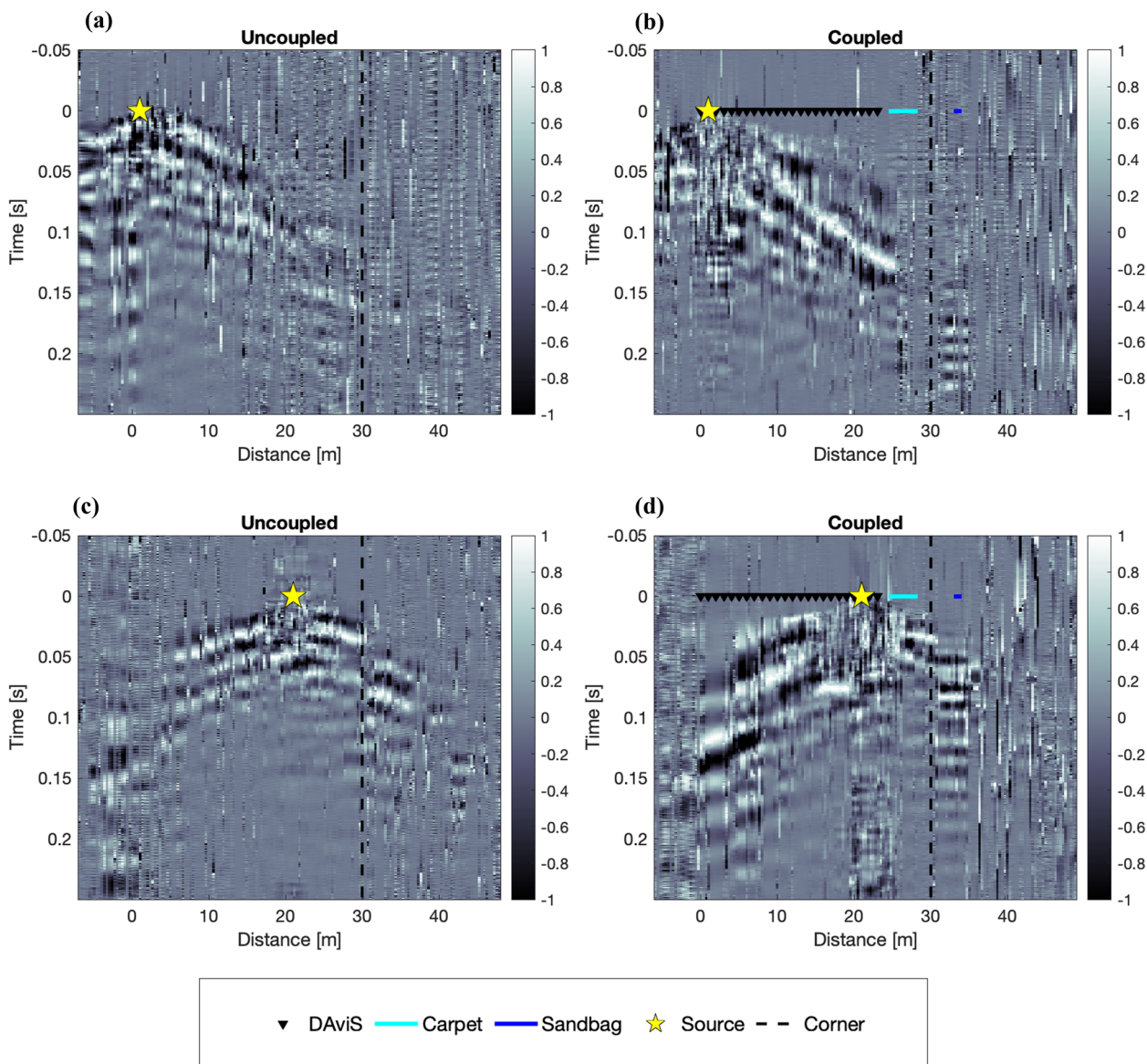


FIGURE 4 Same as for Figure 3, but with each trace normalized to a maximum value of 1. Uncoupled fibre (a, c) profiles and coupled fibre (b, d) profiles for two example shot locations: 1 m (a, b), 21 m (c, d).

the Rayleigh wave coda is likely also due to the direct S-wave that is interfering with the Rayleigh waves in this source–receiver distance range.

Near the source (0–2 m and 20–22 m), the first arriving phases appear to be more coherent in the uncoupled case, but noisy from 0.0–0.075 s over a slightly larger distance range for the coupled cases. This might be caused by the optical phase travelling over multiple fringes at the beginning that are not accurately accounted for by the DAS interrogator. The DAS system may not be able to track the strain variation since the strain rate is too high with the acquisition parameters used. A higher sampling rate may eliminate this issue. Alternatively, the nearfield of the quasi-vertical force source may be complicated and may not generate

horizontal displacements in line with the fibre. This may be exacerbated due to the source being offset slightly from the line.

The unfiltered geophone and DAS waveforms exhibit similar signals, when translated to displacement. Figure 5 shows example waveforms at a source–receiver distance of 19 m. The P-wave is visible on the vertical component (black line), weakly visible on the estimated horizontal component (red line), and visible on the coupled DAS record (blue line). The Rayleigh wave and S-wave arrivals are visible on the vertical, estimated horizontal and coupled DAS records. It is difficult to distinguish between Rayleigh wave and S-wave phases given similar arrival times and interference. The vertical and estimated horizontal components

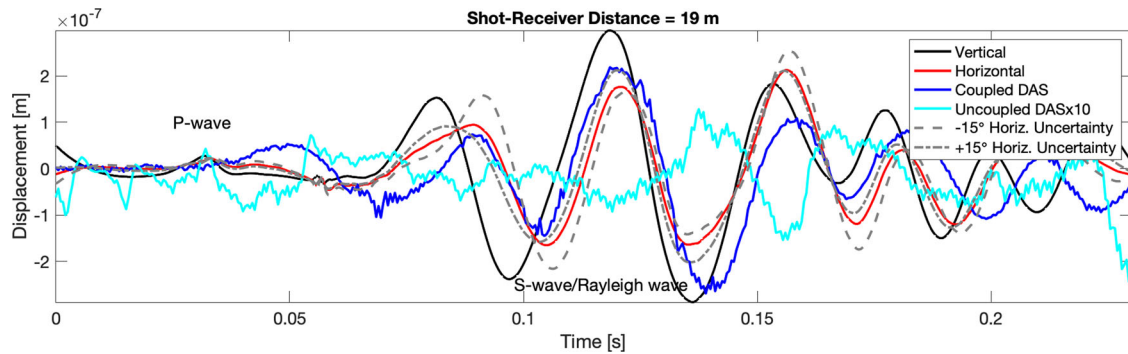


FIGURE 5 Comparison of geophone and DAS waveforms for a source–receiver distance of 19 m. The shot is located at 23 m. Black line shows vertical geophone data, red line shows estimated horizontal component, grey dashed/dotted lines show the variation predicted from errors introduced in the geophone angle of $\pm 15^\circ$, blue line shows coupled DAS displacement data, and cyan line shows the uncoupled DAS displacement data multiplied by a factor of 10. Approximate locations of the P-wave and S-wave/Rayleigh wave are annotated.

are approximately 90° out of phase, as expected for Rayleigh waves. The 90° phase shift is not perfect, likely indicating the interference of the direct S-wave and the Rayleigh wave. The coupled DAS record is roughly in phase with the estimated horizontal geophone component from 0.0–0.2 s. The magnitude of the DAS record is greater than the geophone horizontal record by a factor of 1.1–2.0 between 0.10 s and 0.15 s but has a similar magnitude elsewhere. It does not appear that a simple scalar gain applied to the DAS would suitably correct the records because the difference in amplitude varies with time. The uncoupled DAS record (cyan line) has very low amplitude but has been multiplied by a factor of 10 to aid comparison here. The uncoupled DAS record shows some energy that agrees with the estimated horizontal and coupled DAS record between 0.12 s and 0.17 s with opposite polarity, but otherwise does not resemble the other records at this distance.

The shot sections for the vertical geophone, estimated horizontal geophone and coupled DAS also show many similarities in terms of moveout and phases visible (Figure 6). The first arriving P-wave is visible in all three sections, with a velocity of ~ 1100 m/s. There are also Rayleigh wave phases visible in the sections with a moveout of ~ 330 m/s and S-wave and/or Rayleigh wave phases visible with a moveout of 185 m/s. The phase with a moveout of 185 m/s is visible on the vertical component and may be related to the direct S-wave. The low-frequency Rayleigh waves travel faster than our interpreted S-wave and/or Rayleigh wave phases as they are sensitive to the deeper, faster structure. Multiple modes are likely excited that are interfering, making individual phase identification difficult. This is demonstrated in the modelling work we present below. We do not show other predicted reflections or arrivals in Figure 6 as clear visual identification is difficult. Visual inspection suggests better agreement between the estimated horizontal motion from the geophones and DAS records than

the vertical geophones and the DAS records. The correlation coefficients of the estimated horizontal and vertical components of the geophone data to the coupled DAS records of the shot section (Figure 6) are 0.46 and 0.21, respectively.

We perform refraction analysis and MASW, on the DAS records and geophone data, which essentially yields the same results regarding the 1-D velocity structure. P-wave velocities are determined using a two-layer refraction method using first arrivals (Figure 6). Evaluation of shots at opposite ends of the linear array shows no evidence for dipping layers. The resulting refraction-derived P-wave velocity model has a small layer, 1.2 m, with a velocity of 330 m/s to match the air-wave arrival at near offsets (less than 2 m). At depths of 1.2–6.2 m, the P-wave velocity increases to 1100 m/s (blue line, Figures 6 and 7e). The f - v analysis of a single shot located at 23 m constrains the structure in the upper 15 m (Figure 7). By forward modelling the dispersion curves, as described above in the Methods section, we find S-wave velocities of 185 m/s in the shallowest 6.2 m, increasing to 530 m/s between 6.2 and 9.3 m depth and increasing to 1300 m/s at depths greater than 9.3 m (Figure 7e). We use the P-wave model from the refraction analysis in the forward modelling for the upper 6.2 m and increase the P-wave velocity to 1200 m/s from 6.2–9.3 m depth and to 2420 m/s at depths greater than 9.3 m. The upper 1–6 m has a very high Poisson's ratio, 0.48, which could be consistent with clay-rich material (Gercek, 2007) such as that observed at the site. We note that the f - v analysis of the vertical component has a strong fundamental mode visible (Figure 7a), but the estimated horizontal geophone component and coupled DAS record show both a fundamental mode and higher modes (Figure 7b and d) and, therefore, provide additional constraints on S-wave velocity. The uncoupled DAS shows some of the higher modes, with a very weak to non-existent fundamental mode (Figure 7c).

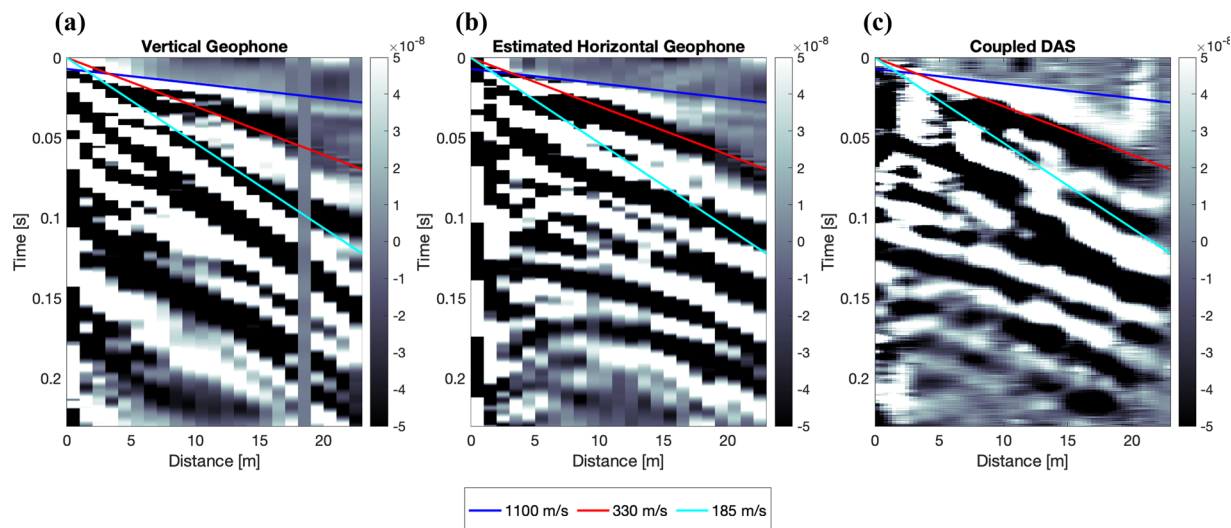


FIGURE 6 Shot sections of a shot at 23 m from the origin for the geophone vertical component (a), horizontal component estimated from the geophone (b), and coupled DAS (c). Distance axis is relative to the shot. Coloured lines indicate moveout velocities of 1100, 330 and 185 m/s, i.e. velocities that might be expected for a P-wave, an S-Wave and/or a Rayleigh wave, respectively.

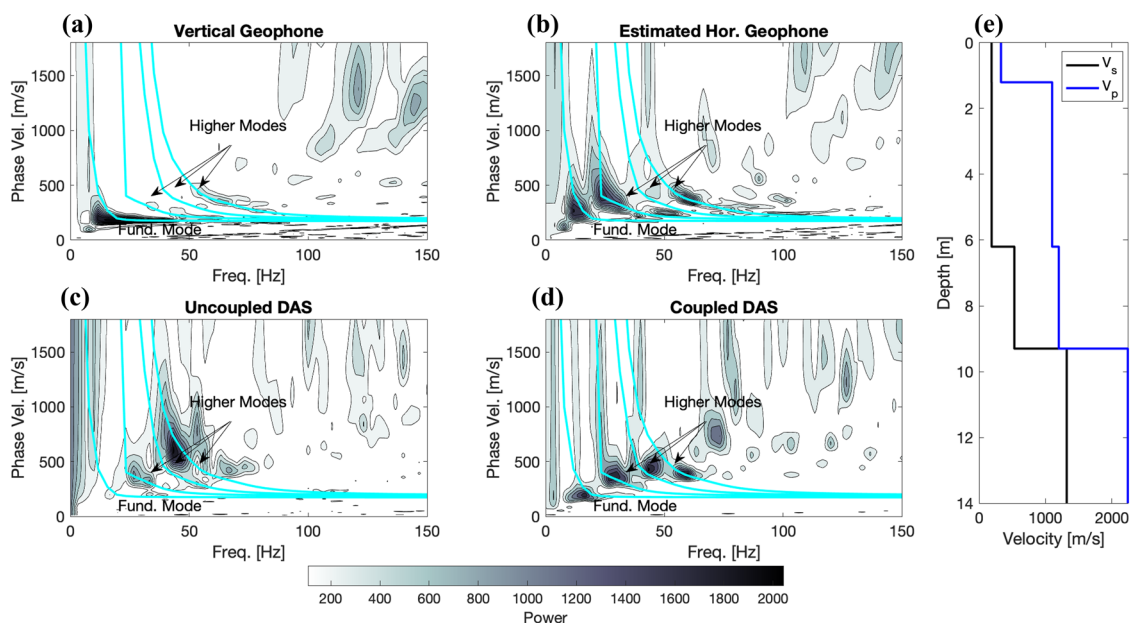


FIGURE 7 $f-v$ analysis of the vertical geophone (a), estimated horizontal geophone (b), uncoupled DAS (c), coupled DAS (d), and best fit forward velocity model (e) for a single shot located at 23 m from origin. In (a–d), darker colours indicate higher likelihood of a phase indicated by greater power in the beamformer output. Dispersion is visible as curved and connected energy. In (e), P-wave (V_p) (blue) and S-wave (V_s) (black) velocity models are shown. The predicted fundamental mode and first three higher mode dispersion curves for the velocity model shown in (e) are indicated by the cyan lines and the modes annotated in (a–d).

Figure 8 shows the average amplitude and phase of the empirical response of the DAS system and the coherence between the DAS and the estimated horizontal displacement for a single shot. We find that the signals are highly coherent between 7.8 Hz and 62.5 Hz, with average coherence values typically higher than 0.8. To estimate the average empirical response, we average

the responses of individual records that had an average coherence of 0.8 or higher between 7.8 Hz and 62.5 Hz. The amplitude of the average empirical response function from 7.8–62.5 Hz ranges from 1.25 ± 0.74 m to 0.33 ± 0.12 m. The phase ranges from $-74^\circ \pm 54^\circ$ to $52^\circ \pm 33^\circ$ over 7.8–62.5 Hz, with error bars in phase that overlap with 0° for most frequencies, except

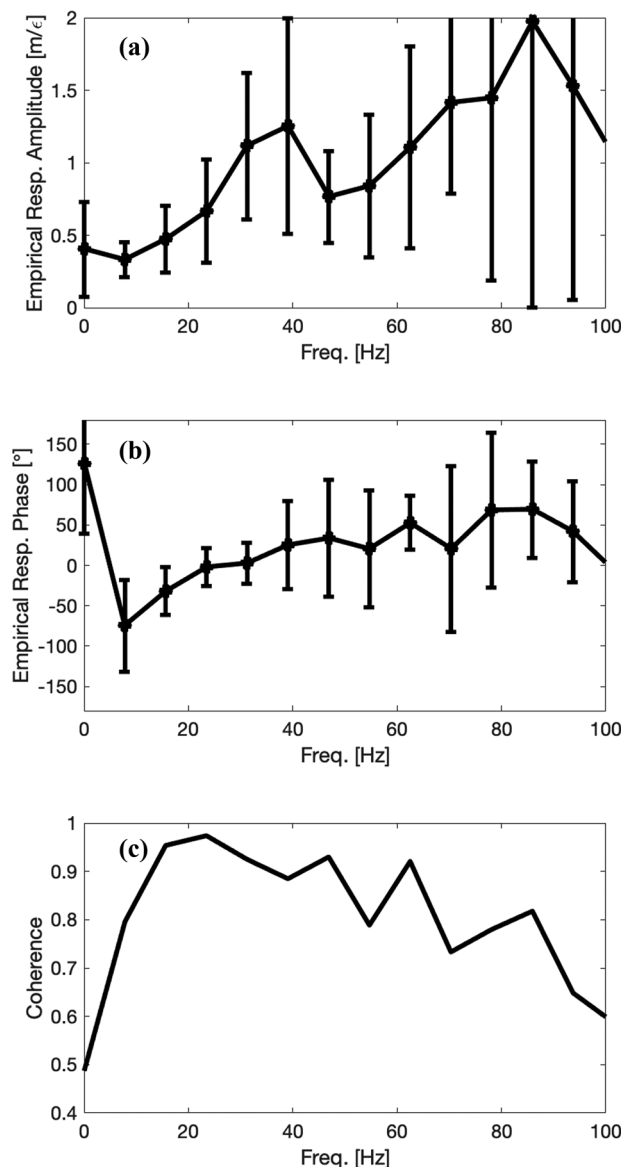


FIGURE 8 Empirical response function and coherence between DAS record and the estimated horizontal component. The records used are from a shot located at 23 m. (a) Empirical response function amplitude. (b) Phase of the empirical response function. (c) Average coherence between the DAS records and estimated horizontal displacement signals

7.8 Hz, 15.6 Hz and 62.5 Hz. Averaging over multiple shot records would likely enhance the estimation of the empirical response function.

DISCUSSION

One of the most surprising observations is that a completely uncoupled fibre can be used to record the ground motion of seismic phases. Although some components of the wavefield are visible, such as the Rayleigh waves, not all phases are clearly visible. For instance, P-waves beyond 16 m from the shot (Figure 3a and c) are less

visible without normalizing the shot section. Surface waves are also visible in the uncoupled DAS records, so MASW could be performed to estimate shallow S-wave velocity structure. The uncoupled DAS for MASW (Figure 7c) yielded similar results to the coupled DAS (Figure 7d), although the fundamental mode was very weak. This suggests that the rapid deployment of fibre and moving closely spaced shots could be an effective strategy for this type of geotechnical work.

Relatively rudimentary and rapid coupling methods are also very effective. The DAViS coupler provides signals that are comparable to the estimated horizontal component geophone data. Specifically, P-waves and the mixed S-waves and Rayleigh waves are visible, including higher modes, using this method. This coupling method can be as fast as deploying geophones or even faster considering there are no additional connections needed for DAS. The DAViS coupler can be used on a variety of substrates. In the present study, we employ the DAViS coupler every 1 m. However, further testing may suggest that coupling might only be needed at a given gauge length to provide effective coupling. The other advantage of optical fibre deployment is that it can be deployed over several kilometres to provide dynamic measurement over thousands of sensing channels.

The carpet coupling is not effective for coupling and may degrade the signal. The wide area and relatively low mass of the carpet used in this test may result in it being supported by the vegetation, thereby decoupling the fibre, if it is mostly in contact with the carpet. In addition, the material properties of the carpeting may act to damp or absorb the signal. A heavier carpet than the one used here may enhance coupling.

The sandbag coupling effectively enhanced the SNR in the region of the fibre where it was deployed, especially in comparison to the uncoupled fibre. The DAS records beneath the sandbag deployed on the W-E segment have different arrival times and a different frequency content than those from the N-S line. This difference is likely caused by directivity related to the 'L'-shaped geometry, which results in different phases being sensed by the different fibre orientations. For instance, horizontally polarized Love waves from our shots have a roughly W-E particle motion, that is, perpendicular to the N-S fibre and parallel to the W-E fibre. These particle motions are better sensed by a fibre in the W-E direction beneath the sandbag. This ambiguity makes direct comparisons between the sandbag and the DAViS coupler challenging. However, previous work shows weighting of the fibre at intervals similar to the gauge length is effective (Spikes et al., 2019), at least for the clay substrate that appears in the photo of this study environment.

The relative merits of pinning the fibre to the ground with a DAViS coupler or weighting using sandbags may depend on the substrate or study area. We expect the grass to make the coupling worse as the grass was

strong enough to lift the fibre away from the ground. The DAViS coupler was effective here. The sandbag may also be a good coupling strategy even in low grass regions like our experiment. In addition, the sandbag may only need to be deployed at every gauge length to ensure good coupling, as implied by the width of high signal (~ 4 m) near the sandbag, relative to the total length of the sandbag (1 m). Heavier sheathing or specialized fibre sheathing (like a weighted tape) could be developed for direct deployment, although this may increase the cost of the fibre. For reference, we use a commercial single telecommunications fibre, which is inexpensive ($\sim \pounds 0.10/\text{m}$) in comparison to a heavily sheathed fibre ($\pounds 2\text{--}3/\text{m}$). Weighting the fibre with sandbags is faster and less invasive, but also heavier, adding to the overall weight of the DAS system for deployments. Pinning the fibre to the ground, on the other hand, does not have the weight penalty, but it is more time consuming. The time required for weighting with a sandbag is about the same time it takes to lay out the fibre as pointed out in the work of Spikes et al. (2019). These weighting methods of deployment may also be ideal for sensitive areas, such as archaeological sites, where disturbing the sub-surface is sometimes forbidden, given that it may harm potential artefacts.

Although we cannot directly compare our results to permanently installed fibre, we find similar variability in SNR and retrieval of P-, S- and surface waves in comparison to previously published work. Two studies of active source shots comparing geophones to buried telecommunication fibre found weak surface wave arrivals on the DAS records in comparison to the geophone data, but good recovery of body waves and reflections (Martin et al., 2017; Zhu et al., 2021). This contrasts with our study, which was dominated by surface wave energy with little evidence for reflections. Another study of buried telecommunications fibre found a good recovery of the fundamental mode and higher mode surface waves in ambient noise correlations as well as body waves from distant earthquake events along some segments of a 101 km of fibre (Ajo-Franklin et al., 2019). Some of the differences in the recovery of surface waves may be attributed to depth variation in the surface wave amplitudes, source excitation and ellipticity due to local structure as well as the coupling of the telecommunications fibre (Lindsey & Martin, 2021).

There are several possible explanations for the difference in amplitude between the estimated horizontal geophone record and the DAS record. First, the response of the estimated horizontal geophone is poorly estimated due to non-linear distortion of the non-vertically deployed geophone. Admittedly, the angle of the geophone deployment is not precise or accurate. Therefore, the absolute amplitude of the estimated horizontal component has a large uncertainty. However, there is some evidence that we are recovering some

amount of horizontal component amplitude, given that the higher mode Rayleigh wave is much more coherent on our estimated horizontal component than on the vertical component (Figure 6). Removing this uncertainty would require using three component seismometers or geophones to better validate the ground motion. Second, the fibre response may not perfectly reflect the Earth's displacement due to its elastic properties (sheathing and the fibre itself). The strain of the fibre depends on the material properties of the fibre itself and the coupling to the sheathing. The material properties of the fibre are well known and are taken into account to estimate the strain calculations, but the effect of the sheathing remains an active area of research (Castongia et al., 2017). Third, imperfect coupling between the fibre and the ground may result in artificial attenuation of the signal as the ground moves more than the fibre. This is certainly the case for the uncoupled fibre experiment, in which the signal attenuates rapidly away from the source. The poor coupling is likely compounded by the vegetation at the experiment site. This may also explain the poor coupling due to the carpet. Its low mass and wide area may effectively couple the fibre to the vegetation rather than to the ground. Finally, the spatial averaging over a gauge length may result in a difference between the displacement estimated from the DAS, and the displacement measured at a geophone/point. Given the lowest velocities (185 m/s) and highest frequency range ($\sim 50\text{--}70$ Hz), which corresponds to a minimum wavelength of 4 m, we do not expect much spatial aliasing based on our gauge length of the DAS system. However, one way to test this would be to use a shorter gauge length closer to the geophone spacing where we might expect the strain to be more uniform.

As discussed above, converting strain to displacement using theoretical relationships does not match the horizontal displacement estimated from the geophones (Daley et al., 2016; Lindsey et al., 2020; Wang et al., 2018), necessitating the calculation of an empirical response function. In our case, even with imperfect coupling, if the assumption of a linear system holds, developing an empirical response function for the 'estimated' horizontal ground displacement and the DAS records may be reasonable. The high coherence in the 7.8–62.5 Hz frequency range suggests that the system is reasonably linear and that the spectral ratio between the estimated horizontal and the DAS records is robust in this range. However, there remains a significant amount of uncertainty in the horizontal displacement and the phase distortion of the geophones.

Our experiment highlights the need for several topics of future work. First, tests on other substrates such as gravel, sand, and thicker vegetation are required to assess the effectiveness of the different coupling strategies examined here. In addition, investigating these different substrates will allow us to determine whether



the response function is universal, or if an empirical response function needs to be acquired for different substrates. Second, detailed comparisons of the response of DAS to three component seismometers or geophones are needed. This will allow us to better evaluate the effectiveness of different coupling methods and the fidelity of the ground motions determined by the DAS systems. Three component instruments will allow us to better identify different seismic phases including Love waves and assess whether DAS systems can be deployed in more complex geometries. Finally, following previous work, assessment of different types of fibre-optic cable sheathings and types over different substrates is needed. Overall, this will allow us to develop optimal strategies and equipment for surface deployments.

CONCLUSIONS

The surface deployment of the fibre-optic cable can record seismic waves from a hammer source in the nearfield (less than 10 m from the source) if completely uncoupled on a grassy field. Better coupling via a DAViS coupler or sandbag, improves the SNR, allowing observation of P-waves, S-waves and Rayleigh waves travelling through the subsurface to at least 23 m away from the source. The phase of the DAS shot records compare well with our estimated horizontal component data, confirming that the fibre records horizontal motions inline of the fibre. Amplitudes of the DAS records and the estimated horizontal components from the geophones are not exactly the same. This is either owing to the uncertainty in the geophone deployment angles or because there is a difference in the response of the fibre relative to the ground motion, possibly related to coupling issues. Future work will require the use of well-calibrated seismometers or geophones to reduce the uncertainty in the response of the DAS system deployed on the surface. Further testing of alternative coupling methods in a variety of substrates will also allow for the development of optimal deployment strategies.

ACKNOWLEDGEMENTS

The authors were partially funded by the Natural Environment Research Council (NE/T005890/1, NE/S012877/1).

DATA AVAILABILITY STATEMENT

Data are available from the authors upon request.

ORCID

Nicholas Harmon <https://orcid.org/0000-0002-0731-768X>

Catherine A. Rychert <https://orcid.org/0000-0001-5071-793X>

Gilberto Brambilla <https://orcid.org/0000-0002-5730-0499>

Yuhang Dai <https://orcid.org/0000-0001-9965-7106>

Petros Bogiatzis <https://orcid.org/0000-0003-1902-7476>

James Snook <https://orcid.org/0000-0002-4636-6548>

Ali Masoudi <https://orcid.org/0000-0003-0001-6080>

REFERENCES

- Ajo-Franklin, J.B., Dou, S., Lindsey, N.J., Monga, I., Tracy, C., Robertson, M. et al. (2019) Distributed acoustic sensing using dark fibre for near-surface characterization and broadband seismic event detection. *Scientific Reports*, 9(1), 1328. <https://doi.org/10.1038/s41598-018-36675-8>
- Bendat, J. & Piersol, A. (2000) *Random data analysis and measurement procedures*, 3rd ed. New York: Wiley and Sons.
- Castongia, E., Wang, H.F., Lord, N., Fratta, D., Mondanos, M. & Chalari, A. (2017) An experimental investigation of distributed acoustic sensing (DAS) on lake ice. *Journal of Environmental and Engineering Geophysics*, 22(2), 167–176. <https://doi.org/10.2113/jeeq22.2.167>
- Chen, M., Masoudi, A. & Brambilla, G. (2019) Performance analysis of distributed optical fiber acoustic sensors based on φ -OTDR. *Optics Express*, 27(7), 9684–9695. <https://doi.org/10.1364/OE.27.009684>
- Claassen, P., Dean, T. & McCarthy, B. (2015) The impact of tilted geophones on land seismic data quality. *ASEG Extended Abstracts*, 2015(1), 1–4. <https://doi.org/10.1071/ASEG2015ab297>
- Cornell, C. (1968) Engineering seismic risk analysis. *Bulletin of the Seismological Society of America*, 58, 1583–1606.
- Daley, T.M., Miller, D.E., Dodds, K., Cook, P. & Freifeld, B.M. (2016) Field testing of modular borehole monitoring with simultaneous distributed acoustic sensing and geophone vertical seismic profiles at Citronelle, Alabama. *Geophysical Prospecting*, 64(5), 1318–1334. <https://doi.org/10.1111/1365-2478.12324>
- Dou, S., Lindsey, N., Wagner, A.M., Daley, T.M., Freifeld, B., Robertson, M. et al. (2017) Distributed acoustic sensing for seismic monitoring of the near surface: a traffic-noise interferometry case study. *Scientific Reports*, 7(1), 11620. <https://doi.org/10.1038/s41598-017-11986-4>
- Freeland, R., Chow, B., Williams, J. & Godfrey, A. (2017) *Relative acoustic sensitivity of standard telecom and specialty optical fiber cables for distributed sensing*. Bellingham, WA: SPIE.
- Gercek, H. (2007) Poisson's ratio values for rocks. *International Journal of Rock Mechanics and Mining Sciences*, 44(1), 1–13. <https://doi.org/10.1016/j.ijrmms.2006.04.011>
- Harmon, N., Gerstoft, P., Rychert, C.A., Abers, G.A., de la Cruz, M.S. & Fischer, K.M. (2008) Phase velocities from seismic noise using beamforming and cross correlation in Costa Rica and Nicaragua. *Geophysical Research Letters*, 35(19), <https://doi.org/10.1029/2008GL035387>
- Herrmann, R.B. (2013) Computer programs in seismology: an evolving tool for instruction and research. *Seismological Research Letters*, 84(6), 1081–1088. <https://doi.org/10.1785/0220110096>
- Jousset, P., Reinsch, T., Ryberg, T., Blanck, H., Clarke, A., Aghayev, R. et al. (2018) Dynamic strain determination using fibre-optic cables allows imaging of seismological and structural features. *Nature Communications*, 9(1), 2509. <https://doi.org/10.1038/s41467-018-04860-y>
- Lindsey, N.J., Dawe, T.C. & Ajo-Franklin, J.B. (2019) Illuminating seafloor faults and ocean dynamics with dark fiber distributed acoustic sensing. *Science*, 366(6469), 1103–1107. <https://doi.org/10.1126/science.aay5881>
- Lindsey, N.J. & Martin, E.R. (2021) Fiber-optic seismology. *Annual Review of Earth and Planetary Sciences*, 49(1), 309–336. <https://doi.org/10.1146/annurev-earth-072420-065213>
- Lindsey, N.J., Rademacher, H. & Ajo-Franklin, J.B. (2020) On the broadband instrument response of fiber-optic DAS arrays. *Journal*

- of *Geophysical Research: Solid Earth*, 125(2), e2019JB018145. <https://doi.org/10.1029/2019JB018145>
- Marra, G., Clivati, C., Luckett, R., Tampellini, A., Kronjäger, J., Wright, L. et al. (2018) Ultrastable laser interferometry for earthquake detection with terrestrial and submarine cables. *Science*, 361(6401), 486–490. <https://doi.org/10.1126/science.aat4458>
- Martin, E.R., Castillo, C.M., Cole, S., Sawasdee, P.S., Yuan, S., Clapp, R. et al. (2017) Seismic monitoring leveraging existing telecom infrastructure at the SDASA: active, passive, and ambient-noise analysis. *The Leading Edge*, 36(12), 1025–1031. <https://doi.org/10.1190/tle36121025.1>
- Masoudi, A., Belal, M. & Newson, T.P. (2013) A distributed optical fibre dynamic strain sensor based on phase-OTDR. *Measurement Science and Technology*, 24(8), 085204. <https://doi.org/10.1088/0957-0233/24/8/085204>
- Masoudi, A. & Newson, T.P. (2016) Contributed review: distributed optical fibre dynamic strain sensing. *Review of Scientific Instruments*, 87(1), 011501. <https://doi.org/10.1063/1.4939482>
- Masoudi, A. & Newson, T.P. (2017) High spatial resolution distributed optical fiber dynamic strain sensor with enhanced frequency and strain resolution. *Optics Letters*, 42(2), 290–293. <https://doi.org/10.1364/OL.42.000290>
- Masoudi, A., Pilgrim, J.A., Newson, T.P. & Brambilla, G. (2019) Sub-sea cable condition monitoring with distributed optical fiber vibration sensor. *Journal of Lightwave Technology*, 37(4), 1352–1358. <https://doi.org/10.1109/JLT.2019.2893038>
- Mestayer, J. et al. (2011) Field trials of distributed acoustic sensing for geophysical monitoring. In: *SEG Technical Program Expanded Abstracts 2011*, pp. 4253–4257. <https://doi.org/10.1190/1.3628095>
- Milne, D., Masoudi, A., Ferro, E., Watson, G. & Le Pen, L. (2020) An analysis of railway track behaviour based on distributed optical fibre acoustic sensing. *Mechanical Systems and Signal Processing*, 142, 106769. <https://doi.org/10.1016/j.ymssp.2020.106769>
- Oppenheim, A.V. & Schaffer, R.W. (1975) *Digital signal processing*. Englewood Cliffs, NJ: Prentice-Hall, Inc.
- Spikes, K.T., Tisato, N., Hess, T.E. & Holt, J.W. (2019) Comparison of geophone and surface-deployed distributed acoustic sensing seismic data. *Geophysics*, 84(2), A25–A29. <https://doi.org/10.1190/geo2018-0528.1>
- Telford, W.M., Geldart, L.P. & Sheriff, R.E. (1990) *Applied geophysics*. Cambridge: Cambridge University Press.
- Templeton, M. (2013) Passive velocity transducer (geophone) response. https://ds.iris.edu/NRL/sensors/sercel/passive_responses.html
- Wang, H.F., Zeng, X., Miller, D.E., Fratta, D., Feigl, K.L., Thurber, C.H. & Mellors, R.J. (2018) Ground motion response to an ML 4.3 earthquake using co-located distributed acoustic sensing and seismometer arrays. *Geophysical Journal International*, 213(3), 2020–2036. <https://doi.org/10.1093/gji/ggy102>
- Yang, J., Shragge, J. & Jin, G. (2021) 4D DAS fiber-coupling effects in freezing near-surface ground conditions. In *First International Meeting for Applied Geoscience & Energy Expanded Abstracts*. Houston, TX: Society of Exploration Geophysicists, pp. 477–482. <https://doi.org/10.1190/segam2021-3582508.1>
- Zhu, T., Shen, J. & Martin, E.R. (2021) Sensing earth and environment dynamics by telecommunication fiber-optic sensors: an urban experiment in Pennsylvania, USA. *Solid Earth*, 12(1), 219–235. <https://doi.org/10.5194/se-12-219-2021>
- Zumberge, M.A., Wyatt, F.K., Yu, D.X. & Hanada, H. (1988) Optical fibers for measurement of earth strain. *Applied Optics*, 27(19), 4131–4138. <https://doi.org/10.1364/AO.27.004131>

How to cite this article: Harmon, N., Rychert, C.A., Davis, J., Brambilla, G., Buffet, W., Chichester, B., Dai, Y., Bogiatzis, P., Snook, J., van Putten, L. & Masoudi, A. (2022) Surface deployment of DAS systems: Coupling strategies and comparisons to geophone data. *Near Surface Geophysics*, 20, 465–477. <https://doi.org/10.1002/nsg.12232>